SUPPORT-BASED DIGITAL AND OPTICAL SUPER-RESOLUTION IN ONE AND TWO DIMENSIONS

Sudhakar Prasad and Xuan Luo
Center for Advanced Studies and Department of Physics and Astronomy
University of New Mexico
Albuquerque, New Mexico 87131

Abstract

We employ a sampling-type expansion of the spatial spectrum of an object brightness distribution supported on a finite, *a priori* known region of space to treat the problem of support-driven superresolution from undersampled image data. The achievable superresolution is quantified in terms of Fisher information and associated Cramér-Rao lower bounds in both the spectral and spatial domains. Unlike most previous theoretical work on the subject, our approach provides a unified analysis of both digital and optical superresolution from low-resolution image sequences, and is not restricted to a specific form of the system transfer functions or to one dimension.

I. Introduction

Improving the resolution of an image beyond that accorded by the image data engages different strategies. Digital superresolution (DSR) overcomes the sampling-limited resolution of the image sensor, e.g., by encoding high-resolution information in a sequence of sub-pixel-shifted but otherwise low-resolution images [1]. DSR cannot, however, yield a true extension of the spatial bandwidth beyond the optical diffraction limit of the imaging system, as one of us argued in Ref.[2] with the help of the Generalized Sampling Theorem.

To achieve optical bandwidth extension, or optical superresolution (OSR), by data inversion one must combine some meaningful *a priori* knowledge with the image data. In fact, all algorithms that claim to achieve OSR incorporate either explicitly or implicitly prior knowledge of one form or another into their data inversion protocol. Enforcing a finite-support constraint in the physical domain is the essential basis of certain OSR algorithms [3–5].

The present work, which corrects and extends our earlier work [2] on 1D OSR, attempts to generalize a large body of research literature [6–11] on the subject of support-constrained OSR over the past four decades. Much of previous work has addressed OSR for a clear-aperture coherent imaging system for which the so-called prolate spheroidal wave functions (PSWF) provide an excellent eigenbasis for formulating the OSR problem. By contrast, the present work is not limited to any specific imaging system, and makes use of sampling-type functions to represent a finite-support object in the spatial-frequency domain. Equally importantly, it provides a unified treatment of subpixel-shift-based DSR and support-based OSR.

Our noise model includes both the additive Gaussian noise of CCD detection and the Possion noise of photon counting. We start with a sequence of sub-pixel-shifted low-resolution (LR) images in which information about the object out to the diffraction limit of the imager can be encoded. We can recover still higher object frequencies by exploiting a prior knowledge of the object support, as we shall demonstrate here. A finite object support couples these latter, superresolving (SR) frequencies lying just beyond the optical band edge into the imager's optical bandwidth, so the image data, in principle, carry information about the SR frequencies. Our Fisher-information (FI) [12] based analysis of the maximum fidelity with which SR frequencies can be estimated will confirm the validity of this argument. We shall treat the OSR problem in the physical domain as well, verifying the previously observed [5, 11] space-variant character of OSR, specifically a higher fidelity of OSR near the support boundaries than well in the interior.

II. Spatial Spectrum of a Finite-Support Object Brightness Distribution

For a space-invariant imaging system with optical PSF given by $h_0(x)$, a continuously defined image, $g(x)$, may be expressed in terms of the object intensity function, $f(x)$, as the convolution

$$g(x) = \int h_0(x - x')\ f(x')\ dx'. \tag{1}$$

Convolving this continuous intensity distribution with the sensitivity function, $p(x - x_k)$, of the kth pixel of the image sensor array, followed by a use of the Fourier convolution theorem, yields for the output count at that pixel the following spatial-frequency integral:

$$g_k^{(m)} = \int du\ \exp[i2\pi u(x_k - t_m)]\ P(-u)\ H_0(u)\ F(u)\ +\ n_k^{(m)}, \tag{2}$$

where $n_k^{(m)}$ is the additive noise at the kth pixel of the mth image, $x_k = k\delta w$ is the position coordinate of the center of the kth pixel in terms of the pixel pitch, δw, and t_m is the sub-pixel shift of the mth image. To maximize the diversity of sub-pixel shifts for optimal high-resolution image reconstruction, they are typically chosen to be regularly spaced fractions between 0 and 1 of the pixel pitch, δw. Upper-case Roman letters denote Fourier transforms of image-domain functions denoted by the corresponding lower-case letters.

Consider first a one-dimensional (1D) imager. For idealized sensor arrays with no dead space between successive pixels and unit quantum efficiency, the pixel transfer function (PTF), $P(u)$, has the form, $P(u) = \delta w\ \mathrm{sinc}(u\delta w)$, where the sinc function is defined as $\mathrm{sinc}(x) \equiv \sin \pi x/(\pi x)$. For a clear aperture, the incoherent OTF is $(1 - |u|/B_0)$, B_0 being the optical bandwidth, and expression (2) may be cast as an integral over the normalized frequency, $\bar{u} = u/B_0$, with all spatial variables scaled by the critical sampling interval, $1/(2B_0)$,

$$g_k^{(m)} = \frac{\chi}{2} \int_{-1}^{1} d\bar{u}\ \exp[i\pi\bar{u}(\bar{w}_k - \bar{t}_m)]\ \mathrm{sinc}(\bar{u}\chi/2)\ (1 - |\bar{u}|)\ F(B_0\bar{u})\ +\ n_k^{(m)}, \tag{3}$$

where $\chi = 2B_0\delta w$ is the ratio of detector-sampling and critical optical-sampling intervals. For $\chi < 1$, the detector oversamples the image while for $\chi > 1$ it undersamples the image.

For a more realistic two-dimensional (2D) imager, we must interpret variables like x and u as appropriate 2D vectors, their product in the scalar-product sense, and 1D line integrals as 2D area integrals. It is easy thus to transcribe our 1D formulation into the correct 2D form. Each Cartesian dimension when occuring separably has its own associated optical and pixel transfer functions. However, because of the extra dimension a number of differences occur too, depending on the geometry of the problem when it is not fully separable in the Cartesian coordinates. Examples of these differences are the form of the OTF, $H_0(u)$, when circular support and/or aperture or non-coaligned rectangular support and aperture geometries are involved, and the specific basis functions for the expansion of the spatial spectrum of the object for such supports.

A 1D object $f(x)$ supported fully on the interval $[-L, L]$ has a Fourier-series expansion,

$$f(x) = \frac{1}{2L} \sum_{\ell=-\infty}^{\infty} F_\ell \exp(i\pi\ell x/L), \quad \text{with } F_\ell = \int_{-L}^{L} f(x)\ \exp\{-i2\pi[\ell/(2L)]x\}\ dx. \tag{4}$$

The Fourier transform (FT) of this expansion yields the full object spectrum, $F(u)$, in terms of its spatial-frequency samples, $F_\ell = F(u = \ell/2L)$, as

$$F(u) = \sum_{\ell=-\infty}^{\infty} F_\ell\ \mathrm{sinc}(2uL - \ell), \tag{5}$$

much like the usual Shannon-Nyquist expansion for a band-limited function in terms of its critical spatial samples. The implication of this expansion for the imaging equation (3) is that the information in the spatial-frequency samples outside the measurement band, $[-B_0, B_0]$, is aliased into the measurement band and thus in principle contained in the acquired data. The finiteness of the support is directly responsible for this aliasing. Note, however, that because the width of the sinc function in Eq. (5) is of order $1/(2L)$, the maximum bandwidth extension that can be expected is also of that order. This is consistent with previous results on unbiased, primary OSR [10, 13].

The 2D analog of this expansion for a rectangular support of size $L_1 \times L_2$ uses the Cartesian tensor-product basis,

$$F(u_1, u_2) = \sum_{\ell_1=-\infty}^{\infty} \sum_{\ell_2=-\infty}^{\infty} F_{\ell_1\ell_2}\ \mathrm{sinc}(2u_1L_1 - \ell_1)\,\mathrm{sinc}(2u_2L_2 - \ell_2), \tag{6}$$

where $F_{\ell_1\ell_2} = F(u_1 = \ell_1/(2L_1), u_2 = \ell_2/(2L_2))$ are the regularly spaced samples of the object spectrum.

By contrast, when the object distribution is supported on a circular disk of radius a, it is best treated via the Fourier-Bessel basis functions,

$$f(\rho, \phi) = \sum_{m=-\infty}^{\infty} \sum_{n=1}^{\infty} F_{mn}\ \Psi_{mn}(\rho, \phi), \quad \text{with } F_{mn} = \int f(\rho, \phi)\ \Psi_{mn}^*(\rho, \phi)\ d^2\rho, \quad 0 \le \rho < a, \tag{7}$$

where the basis functions are defined as [14]

$$\Psi_{mn} = \frac{J_m(x_{mn}\rho/a)\exp(im\phi)}{\sqrt{\pi a^2}J_{m+1}(x_{mn})} \tag{8}$$

in terms of the nth positive zero, x_{mn}, of the Bessel function J_m. That this is an optimal basis for analyzing bandwidth extrapolation for circular supports is evidenced by the fact that the coefficients F_{mn} are directly related to the spatial spectrum of the object. Specifically, F_{mn} may be shown [15] to be proportional to the mth azimuthal Fourier component of the spatial spectrum of the object, evaluated at the spatial frequency $u = x_{mn}/(2\pi a)$. For large n, the zeros x_{mn} are nearly regularly spaced. Note that unlike the PSWFs, our choice of basis functions, whether in 1D or for different 2D geometries, is not linked to any specific OTFs.

A 2D Fourier transform of Eq. (7) generates the spatial spectrum of the object brightness distribution. After some tedious but straightforward algebra, we may derive [15] the following expansion of the spatial spectrum in terms of the Fourier Bessel samples:

$$F(\mathbf{u}) = \sum_{mn} F_{mn}(-i)^m \sqrt{4\pi a^2} \frac{x_{mn}}{(x_{mn}^2 - 4\pi^2 u^2 a^2)} J_m(2\pi u a)\ \exp(im\phi_u). \tag{9}$$

Note that the function multiplying F_{mn} in the above double sum is the 2D circular-support analog of the 1D sinc function of expansion (5). Eqs. (5), (6), and (9) serve as the essential basis of our support-enabled-OSR analysis.

III. Fisher Information and 1D Superresolution

Use of expression (5) in Eq. (2) yields the following image data value in terms of the object spatial-frequency samples:

$$g_k^{(m)} = \sum_{\ell=-\infty}^{\infty} c_{k\ell}^{(m)} F_\ell + n_k^{(m)}, \tag{10}$$

with

$$c_{k\ell}^{(m)} = \frac{\chi}{2} \int_{-1}^{1} du\ (1 - |u|)\ \mathrm{sinc}(\chi u/2)\ \exp[i\pi u \chi\,(k - \bar{t}_m)]\ \mathrm{sinc}(Q(u - \ell/Q)), \tag{11}$$

where $Q = 2LB_0$ is the space-bandwidth product (SBP) and $\bar{t}_m = 2B_0 t_m/\chi$ is the mth image shift expressed as a fraction of the detector-pixel width. Since the successive samples, F_ℓ, are $1/(2L)$ apart in spatial frequency, those samples whose ℓ index exceeds Q in magnitude lie outside the optical passband of the imager and are thus the superresolving (SR) frequencies. We truncate the above infinite sum at finite upper and lower limits, $\pm\eta Q$, where η when it exceeds 1 represents the degree of sought OSR. As η increases beyond 1, it becomes increasingly difficult to recover the highest SR frequencies from noisy image data because of the rapidly decaying tail of the sinc aliasing function in Eq. (11).

A lower bound on the sum of variances for estimating the real and imaginary parts of a complex parameter like F_ℓ, sometimes called its pseudo-variance, is given by the corresponding diagonal element of the inverse of a complex Hermitian Fisher Information (FI) matrix. The $\ell\ell'$ element of the FI matrix is defined as the statistical self-average

$$J_{\ell\ell'} = \left\langle \frac{\partial \ln P}{\partial F_\ell} \frac{\partial \ln P}{\partial F_{\ell'}^*} \right\rangle, \tag{12}$$

where P stands for the probability distribution (PD) of data, given F, and triangular brackets indicate averaging of the quantity they enclose over the same PD. Because of the reality condition, $F_\ell^* = F_{-\ell}$, it is sufficient to consider only non-negative ℓ, ℓ' values when considering the matrix elements of $\mathbf{J}$.

In the presence of combined additive sensor noise and Poisson noise of counting, the preceding average is evaluated easily in terms of the coefficients, $c_{k\ell}^{(m)}$,

$$\mathbf{J} \approx \sum_{m,k} \frac{\underline{c}_k^{(m)} \underline{c}_k^{(m)\dagger}}{\sigma_D^2 + \left\langle g_k^{(m)} \right\rangle}. \tag{13}$$

where $\underline{c}_k^{(m)}$ is a column vector with ℓth element being equal to $c_{k\ell}^{(m)}$ and σ_D^2 is the additive noise variance per sensor pixel. The other term in the denominator, namely $\left\langle g_k^{(m)} \right\rangle$, represents the variance of the Poisson count statistics, which we treat here only approximately via a quasi-Gaussian probability density function (PDF). Because of the sum

form (13) of the FI matrix, its maximum possible rank is equal to the number of terms in the sum, namely the product of the number of images and the number of detector pixels per image. This is to be expected since the data-based FI matrix contains only as much information as has been acquired through measurements. We must therefore have at least as many independent data points as the matrix dimension, namely $\eta Q + 1$, so the FI matrix is full-rank and can be inverted to yield sensible CRBs which we discuss next.

IV. Numerical Results and Discussion of 1D OSR

We now illustrate several essential features of the CRB for a joint, unbiased estimation of the spatial frequencies of two different classes of objects, namely centered Gaussian objects and objects containing only three pure sinusoidal frequencies, both constrained on the spatial interval $(-L, L)$ in 1D. A typical object of each kind, along with its LR image for $Q = 20$, is shown in Fig. 1. The frequency index, ℓ, was chosen to run over the set of integers, $\{0, 1, \ldots, \ell_{max}\}$,

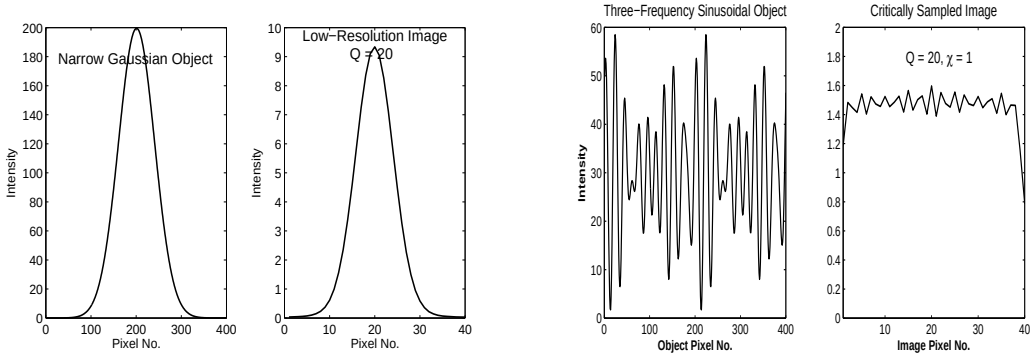

(a)Gaussian source with $w = 0.2$

(b)Sinusoidal source with three pure frequencies, 8, 9, and 11

FIG. 1: Two typical sources and their unshifted LR images for $Q = 20$

for two values of Q, namely 5 and 20. In our numerical calculations of the exact expression (13) for the FI and its inverse, the set of jointly estimated samples was enlarged incrementally by adding the next higher-frequency sample pair at a time, *i.e.,* by incrementing ℓ_{max} by 1 each time. Three values of ℓ_{max}, namely Q, $Q + 1$, and $Q + 2$, were considered corresponding to the inclusion of zero, one, and two pairs of samples outside the measurement bandwidth, respectively. We first considered only one ($M = 1$) critically sampled ($\chi = 1$) LR image, rather than a sequence of multiple images, in order to focus exclusively on OSR.

In Figs. 2, we plot the normalized CRB for the Gaussian object of two different width-parameter values, $w_0 = 0.1$ and 0.5, for $Q = 20$. The peak SNR, defined as the ratio of the maximum object intensity to the standard deviation, σ_D, of the additive noise, was taken to have two different values, namely 10^3 (bright-source limit, upper figures) and 10 (moderately bright source, lower figures). In the higher-SNR case, the Poisson noise of counting dominates the additive noise, while for the lower-SNR case the two noise sources are generally comparable over the majority of the image pixels. Before plotting the CRBs, we normalized them by dividing them by the square of the mean photon number at the brightest object pixel. A number of important observations may be made. First, for the lower-SNR case, the prior knowledge of support provides significantly more information for the larger-width Gaussian than for the narrower-width Gaussian, the image for the latter dropping in intensity to sensor noise levels well before the support boundaries are reached. This is seen in the sharply lower normalized CRBs for the former (lower left) than for the latter (lower right). Second, in the bright-source limit, the support information is most effective when the object spectrum has both significant value and slope at the band edge, since then the aliasing of SR frequencies into the optical passband is not only significant but also permits their disambiguation. This situation occurs for the narrower-width Gaussian, for which the normalized CRBs are generally a factor of about 2-5 lower than for the larger-width Gaussian. Third, for both SNR values the CRBs rise sharply for the SR frequencies, although the CRBs for the data-resolved (DR) frequencies seem more or less unchanged regardless of how many SR frequencies are estimated.

An important motivation for our present work has been to advance an integrated treatment of digital and optical superresolution (DSR and OSR) when images are in general undersampled by the detector pixels. For critically sampled images, the use of more than one image, say M images, merely reduces the relative variance of estimation noise by a factor M corresponding to the standard noise reduction due to multiple independent measurements. This can be seen in Figs. 3 for the case of $Q = 5$ and additive-noise-dominated estimation, for which the peak SNR was chosen to be 10^{-3}. The left panel shows the normalized CRB for a single critically sampled image ($\chi = 1,\ M = 1$),

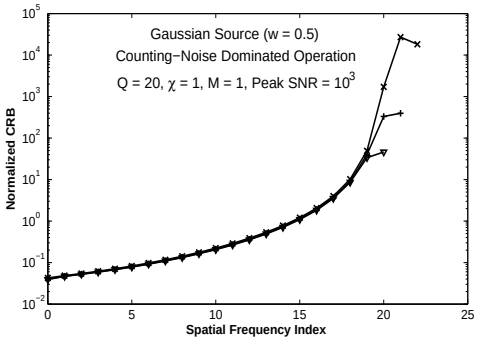

(a)$w = 0.5$, Peak SNR = 10^3

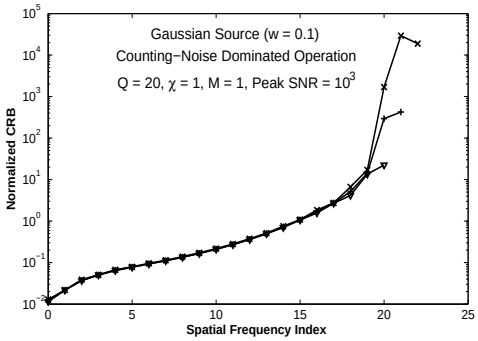

(b)$w = 0.1$, Peak SNR = 10^3

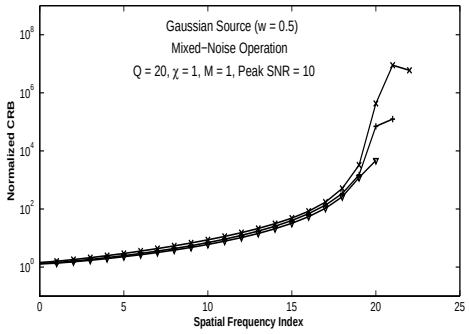

(c)$w = 0.5$, Peak SNR = 10

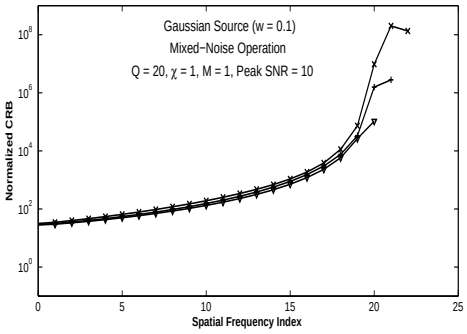

(d)$w = 0.1$, Peak SNR = 10

FIG. 2: Normalized CRB for a Fourier sample plotted vs the index of the sample, for $Q = 20$, two different Gaussian widths, $w = 0.5$ and 0.1, and two peak SNR values, 10^3 and 10.

while the right panel shows the normalized CRB using five ($M = 5$) critically sampled images. The factor-M reduction is easily seen between the two sets of plots.

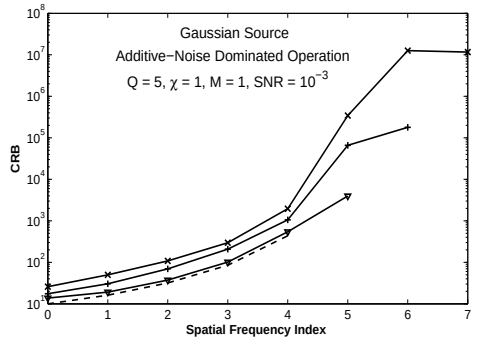

(a)$Q = 5$, $\chi = 1$, $M = 1$, Peak SNR = 0.001

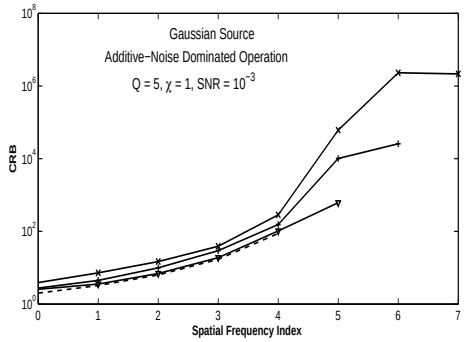

(b)Same as Fig. 3(a) except $M = 5$

FIG. 3: Normalized CRB plotted vs index of the frequency sample, for critically sampled images of a wide Gaussian source ($w = 1$).

The availability of multiple sub-pixel-shifted LR images should provide for nontrivial DSR when these images are undersampled ($\chi > 1$) by the detector. We show this in the next set of figures for which the (χ, M) pair equals (2,5) (Fig. 4(a)), (5,5) (Fig. 4(b)), and (5,2) (Fig. 4(c)). As the number, M, of sub-pixel-shifted LR images is increased above χ, keeping everything else unchanged, the normalized CRBs go down merely by the factor M/χ reflecting a simple noise averaging that results from multiple redundant measurements, as we saw in Figs. 3. By contrast, as the last figure (Fig. 4(c)) in this set shows, having fewer images than the undersampling factor, *i.e.,* $M < \chi$, in a joint estimation of data-resolved (DR) and SR frequencies dramatically increases the noise of estimating even the DR

frequencies that would be normally resolved by the detector. One thus must have $M \geq \chi$ in order to have the ability to recover all of the DR frequencies. These considerations underscore the fact that the number of indepedent spatial degrees of freedom for a support-limited, band-limited imaging environment is given by the total number of critical samples, spaced consecutively by distance $1/(2B)$ over the spatial support, $2L$, of the object, namely $2Q$, as has been widely recognized before [6, 7, 10].

The cusps seen in the curves on Fig. 4(b) at $\ell = 8$ and 16 are due to the reduced information at spatial frequencies that are multiples of $2/\chi$ (times B) where the detector PTF vanishes identically. Without any support-based convolutions in the spatial-frequency domain, these frequencies would have infinite CRBs (i.e., no data sensitivity); any information about them carried by the data is then solely due to the prior knowledge of the object support. Whenever $\chi > 2$, the corresponding CRB plots exhibit cusp-like behavior at those spatial frequencies whose index ℓ is an integral multiple of $\ell_0 \equiv 2Q/\chi$.

In all of our figures containing CRB plots it is quite clear that the minimum noise variance of adding a single pair of SR spatial frequencies to the reconstructed image, *i.e.,* increasing ℓ_{max} by 1, is essentially a constant factor, of order 10^2, larger than before. This corresponds to a logarithmic scaling of the number of estimated SR frequencies with image SNR, whether in the additive or Poisson-noise-dominated regime, a conclusion reached by previous researchers too [10, 11, 13].

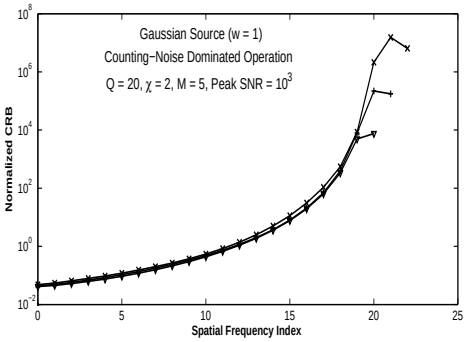

(a)$Q = 20$, $\chi = 2$, $M = 5$, Peak SNR $= 10^3$

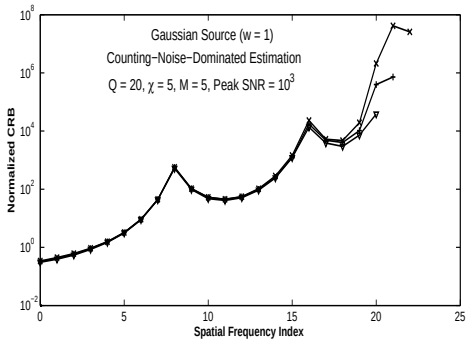

(b)Same as Fig. 4(a), except $\chi = 5$

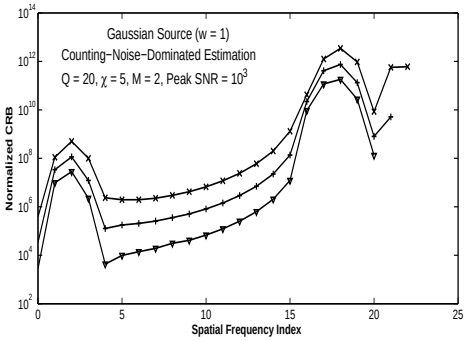

(c)Same as Fig. 4(b) except $M = 2$

FIG. 4: Normalized CRB for a Fourier sample plotted vs the index of the sample for $Q = 20$, for different values of the undersampling factor χ and the number of LR images.

Many of the conclusions drawn from the preceding figures are qualitatively independent of the detailed intensity profile of the source under consideration. We repeated our study with sources that contain only a few purely sinusoidal waveforms along with the dc term, corresponding to the presence of only a handful of Fourier spatial frequencies. Without finite support boundaries, such sources would have infinite extension, so the knowledge of the support does provide useful information, particularly in the moderate-SNR regime, when one or more of the source frequencies lie just outside the optical band edge. This was verified in our analysis. For the sake of brevity we do not display these results here.

V. Numerical Results and Discussion of 2D OSR

We shall present here our results for the case of circular support only, deferring the presentation of results for the simpler rectangular support geometry to the conference talk. Qualitatively similar results were obtained for both 2D geometries, but they do differ from the corresponding results in the 1D case in an essential way. Specifically, one may show [15] that the FI matrix elements are typically of order $1/Q^2$, where $Q \equiv 2B_0 a$, for 2D as opposed to order $1/Q$ for the 1D case. Thus, the CRBs, given by the inverse FI matrix, scale as Q^2 which represents the 2D space-bandwidth *area* product. Estimating even the data-resolved frequencies can thus be a far noisier proposition, making OSR much harder to achieve, in 2D than in 1D for large enough Q.

A measure of the brightness of the source, somewhat superior to the peak SNR for present purposes, is the ratio, NR, of maximum-brightness image pixel intensity to the additive detector noise variance per pixel, namely σ_D^2. The next set of figures display CRB for the FB samples of a bright (NR = 100) circular-disk-supported elliptical Gaussian object of form,

$$f(x,y) = K\ \exp[-(\alpha x^2 + \beta y^2)]\ \Theta\left(a - \sqrt{x^2+y^2}\right), \tag{14}$$

where Θ denotes the Heavyside unit step function. For these plots, the radius, a, of the circular support disk and the ellpse parameters, α and β, were chosen to be 1, 2, and 8, respectively. We display the normalized CRBs for estimating FB samples with the spatial-frequency cutoff chosen at $(Q + \Delta Q)/(2a)$. OSR may be regarded as the process by which Q is in effect increased by some finite amount ΔQ. The different curves in Figs. 5 (a) and 5(c) are plots of the normalized CRB vs. the radial index n of the FB sample, for different values of its azimuthal index, m, and $\Delta Q = 2$. Figs. 5(b) and 5(d) display the same results slightly differently by plotting the Bessel zero x_{mn}, which is $2\pi a$ times the spatial frequency of the (mn)th FB sample, rather than its index n, on the abscissa. We note that doing this brings the various CRB curves, which do not overlap in the former plots, into approximate coincidence, at least over the mid-frequencies. For sufficiently large Q, the CRBs depend, to an excellent approximation, only on the spatial frequency of the FB samples, not on their azimuthal or radial indices, m, n.

In Figs. 5, we chose the undersampling factor, χ, to be 2, and correspondingly included 2×2, or 4, LR images for which a combination of DSR and OSR is needed to achieve true bandwidth extrapolation. By comparison, Fig. 6(a) corresponds to the use of a single critically sampled image, $\chi = 1$, with all other parameters held the same as in Fig. 5(d). A quick comparison of these two figures reveals the additional noise cost associated with DSR when $\chi = 2$, which raises the CRBs by a factor of 2-3 over the full range of FB samples.

In Fig. 6(b), we show the case of a smaller bandwidth extrapolation, that corresponding to raising the effective Q by 1, $\Delta Q = 1$, using data from four x2 undersampled LR images at $Q = 20$. A comparison with Fig. 5(d) shows roughly a x50 reduction for the largest CRB values when $\Delta Q = 1$. This fact provides strong evidence for the extremely high data SNR required to achieve even modest OSR.

VI. FI and CRB in the Physical Image Plane

Since the FB transform connects the physical-plane brightness distribution to its FB samples, the FI matrix in the FB-transform domain considered so far is related to that in the physical domain by a second-rank complex tensor transformation. However, in order to be able to invert the FI to compute the CRBs, we must ensure that this linear transformation is also invertible. This is done by choosing the same number of discrete samples in the physical domain as the number of FB transform coefficients relative to which the FI is computed. The choice of the physical-domain (PD) samples is somewhat arbitrary unlike the 1D case where physical and Fourier-domain samples are tightly defined via the FFT and periodic boundary conditions.

The FI relative to the PD samples has matrix elements

$$J^{(ph)}_{\ell k;\ell' k'} \equiv \left\langle \frac{\partial \ln P}{\partial f_{\ell k}} \frac{\partial \ln P}{\partial f_{\ell' k'}} \right\rangle, \tag{15}$$

where the superscript ph denotes PD quantities, $f_{\ell k} \equiv f(\rho = \rho_\ell, \phi = \phi_k)$ are the PD samples evaluated at polar-coordinate positions (ρ_ℓ, ϕ_k), and we have exploited the fact that the PD samples are real to dispense with any complex conjugation of the second factor inside the average (15). By means of the chain rule for partial derivatives,

$$\frac{\partial \ln P}{\partial f_{\ell k}} = \sum_{mn} \frac{\partial \ln P}{\partial F_{mn}} \frac{\partial F_{mn}}{\partial f_{\ell k}}, \tag{16}$$

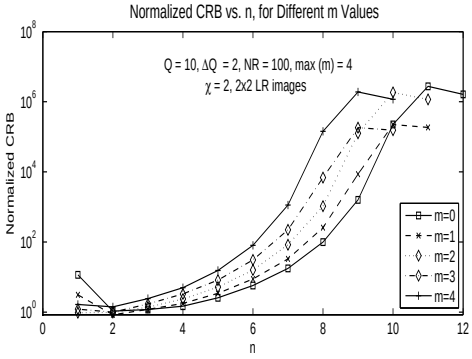

(a)$Q = 10$, $\Delta Q = 2$, $\chi = 2$, NR $= 100$, CRB vs. n

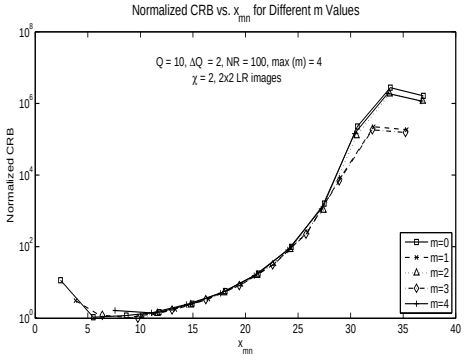

(b)Same as Fig. 5(a), except CRB vs. x_{mn}

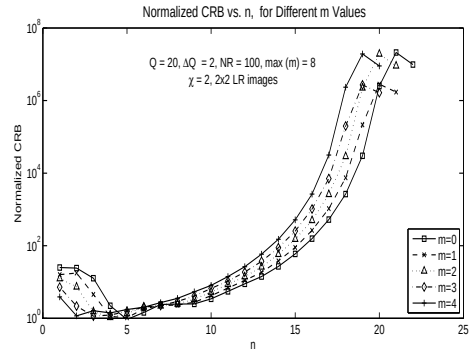

(c)Same as Fig. 5(a) except $Q = 20$

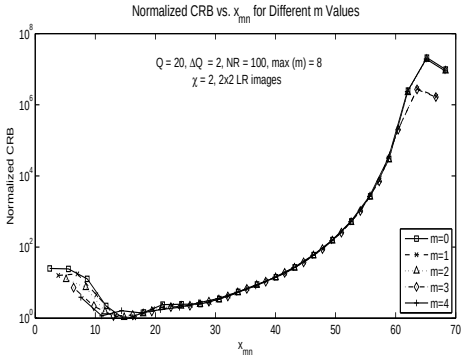

(d)Same as Fig. 5(b) except $Q = 20$

FIG. 5: Normalized CRB for Fourier Bessel (FB) samples for $Q = 10$ and $Q = 20$ and $\chi = 2$.

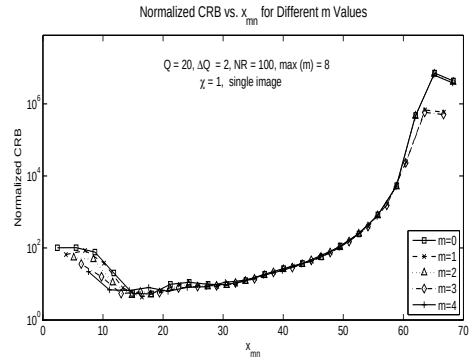

(a)$Q = 20$, $\Delta Q = 2$, $\chi = 1$, NR $= 100$, CRB vs. x_{mn}

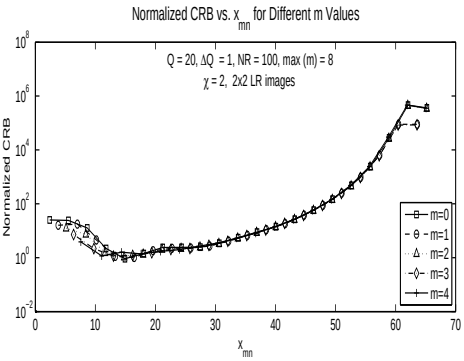

(b)Same as Fig. 5(d), except $\Delta Q = 1$

FIG. 6: Normalized CRB for Fourier Bessel (FB) samples for $Q = 20$ and $\chi = 1$.

we may relate the FI matrix elements, (15), in the physical domain to those in the FB domain by the following sum over two pairs of indices, m, n and m', n':

$$J^{(ph)}_{\ell k;\ell' k'} = \sum_{mn} \sum_{m'n'} T_{\ell k;mn} J_{mn;m'n'} T^*_{\ell' k';m'n'} \tag{17}$$

where T denotes the linear transformation between the two domains, with elements

$$T_{\ell k;mn} \equiv \frac{\partial F_{mn}}{\partial f_{\ell k}}. \tag{18}$$

Relation (17) may be interpreted simply as a generalized matrix product relation, $\mathbf{J}^{(ph)} = \mathbf{TJT}^*$. Its inverse is thus the product of the inverses of these matrices taken in the reverse order. Being the diagonal elements of the inverse FI

matrix, the CRBs in the physical domain are thus given by the following "double"-sum relation:

$$CRB_{\ell k}^{(ph)} = \sum_{mn} \sum_{m'n'} S^*_{\ell k;mn} \mathbf{J}^{-1}_{mn;m'n'} S_{\ell k;m'n'}, \tag{19}$$

where in view of the definition (18) of the forward transformation coefficients and the FB-transform relation (7) the inverse transformation coefficients may be expressed as

$$\begin{aligned} S_{\ell k;mn} &= \frac{\partial f_{\ell k}}{\partial F_{mn}} \\ &= \Psi_{mn}(\rho_\ell, \phi_k) = \frac{J_m(x_{mn}\rho_\ell/a)\exp(im\phi_k)}{\sqrt{\pi} a J_{m+1}(x_{mn})}. \end{aligned} \tag{20}$$

We choose the image-plane samples to be uniformly spaced along the radial and angular dimensions, namely

$$\rho_\ell = \frac{\ell}{L}a, \quad \ell = 1, \ldots, \text{int}(L); \quad \phi_k = \frac{2\pi}{M+1}m, \quad m = 0, \pm 1, \ldots, \pm M, \tag{21}$$

where $(2M+1)$, as before, is the same as the number of m samples in the FB-transform domain, and $\text{int}(L)$ is the largest integer smaller than L. Fixing L requires that the total number of 2D samples, $(2M+1)L$, be the same as the total number of mn samples chosen in the FB-transform domain, *i.e.*, $L = \sum_m n_{max}(m)/(2M+1)$.

The sum over mn and $m'n'$ involves both positive and negative values of m and m' for which, because of the reality of expression (7) and $\Psi^*_{mn} = \Psi_{-mn}$, the FB-transform samples are complex conjugates of each other, $F_{-mn} = F^*_{mn}$. This means that the FI matrix elements considered in the previous section over only the non-negative integer values of m and m' must be first extended to include all positive and negative integer values between $-M$ and M. Extending the m and m' values to include negative integers also essentially doubles the number of rows and columns of the original FI matrix defined in Eq. (12). Use of a 2D $\rightarrow$ 1D lexicographic mapping of index pairs like mn and ℓk allows all sums involved in Eq. (19) to be performed as ordinary matrix operations in Matlab. Undoing this mapping returns us to the physical 2D plane.

In Figs. 7, we display for $Q = 20$ the image-domain CRBs for a bright single-Gaussian source when the ratio of the peak value of the mean count and the detector noise variance is large at 100. The two subfigures refer to two different cases of OSR, namely $\Delta Q = 1, 2$. Like the CRBs in the FB-transform domain, the CRBs in the spatial domain also rise dramatically with increasing ΔQ values. One of the most prominent features of these plots is that the CRB values vary relatively slowly over pixels that are far away from the support boundary. The double sum over all image pixels of all LR images involved in the FI matrix elements (13) tends to smooth out variations in the image intensity from pixel to pixel. However, the CRBs near the support boundary are about 4 orders of magnitude smaller than those near the center of the support. The information in the support is more effective for pixels near its boundary as a result of correlation of perfect information in the strictly zero-valued pixels at and outside the boundary with those close but inside the boundary. This spatially inhomogeneous behavior of the CRB was also clearly present in our 1D analysis, and has been observed by many others previously in both theory and simulation.

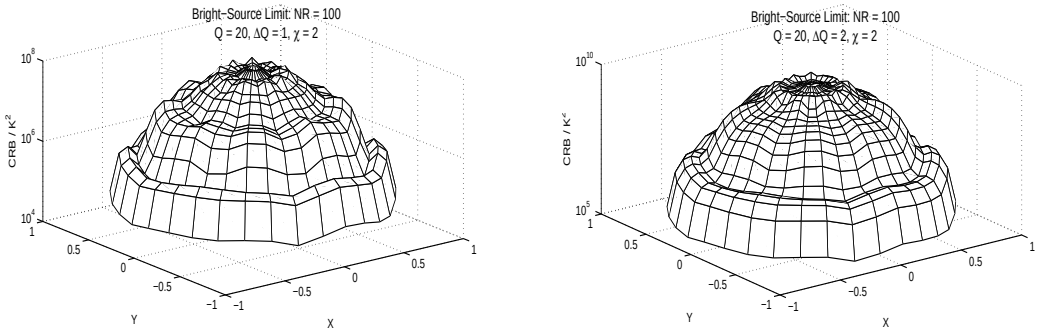

(a)$Q = 20$, $\Delta Q = 1$, $\chi = 2$, NR = 100 (b)Same as Fig. 7(a), except $\Delta Q = 2$

FIG. 7: Normalized CRB for image-plane samples of a bright single-Gaussian object for $Q = 20$, $NR = 100$, and $\chi = 2$.

VII. Conclusions

This paper has explored estimation-theoretic limits on the extent of spatial bandwidth extrapolation from a set of sub-pixel-shifted undersampled images based on a prior knowledge of the object support in one dimension. Our approach makes use of appropriate sampling-type basis sets in the spatial-frequency domain to expand the spatial-frequency amplitude of the object intensity distribution in terms of certain discrete spatial-frequency samples. Such expansions encapsulate essential information about the SR frequencies conferred on the image data by the object support via a convolution of the object and support spectra.

While this problem has been studied extensively over the past four decades, the present work further clarifies the essential principles behind OSR and theoretical upper bounds on it when the support of the object brightness distribution is known in advance. Like the work of Matson and Tyler [11], we have exploited the concept of FI and associated error lower bounds to characterize a fundamental estimation-theoretic limit on the fidelity of performing any bandwidth extension. Such error bounds were computed for unbiased estimation and illustrated with a number of detailed figures both in the spatial-frequency and image domains. Most practical image reconstructions from statistical image data are biased estimations with typically far lower errors, however, so the results presented here give us confidence that OSR from image data is not entirely hopeless even when the size of the object is its only additional property known *a priori*.

Our analyses of two-dimensional images supported on a rectangle via a double Fourier-series expansion leading to the spectral expansion (6) and on a circular disk via the Fourier-Bessel expansion (7) can be generalized further to an arbitrary support geometry by numerically constructing analogous basis functions appropriate to that geometry. A convenient approach for constructing such basis functions may employ a variational formulation in which one minimizes the expectation value of a positive operator in the space of trial basis functions, subject to certain boundary conditions.

Acknowledgments

This work was inspired by numerous discussions on the subject of optical superresolution with Professor M. Fiddy in a number of program-review workshops held under the PERIODIC project. The research was supported in part by IARPA and executed under contract with DMEA, and by AFOSR under grant no. FA9550-08-1-0151.

---

[1] S. Prasad, "Digital superresolution and the generalized sampling theorem," J. Opt. Soc. Am. A, vol. A 24, pp. 311-325 (2007)

[2] S. Prasad, "Digital and optical superresolution of low-resolution image sequences," Unconventional Imaging Conference, 2007 Annual SPIE Meeting, San Diego, CA, Aug 25-29, 2007: Proc. SPIE, vol. 6712, pp. 67120E 1-11 (2007).

[3] R. Gerchberg, "Superresolution through error energy reduction," Opt. Acta, vol. 21, pp. 709-721 (1974).

[4] A. Papoulis, "A new algorithm in spectral analysis and band-limited extrapolation," IEEE Trans. Circuits Syst., vol. CAS-22, pp. 735-742 (1975).

[5] S. Plevritis and A. Macovski, "Spectral extrapolation of spatially bounded images," IEEE Trans. Medical Imaging, vol. 14, pp. 487-497 (1995).

[6] C. Rushforth and R. Harris, "Restoration, resolution, and noise," J. Opt. Soc. Am., vol. 58, pp. 539-545 (1968).

[7] G. Toraldo Di Francia, "Degrees of freedom of an image," J. Opt. Soc. Am., vol. 59, pp. 799-805 (1969).

[8] B. R. Frieden, "Evaluation, design, and extrapolation methods for optical signals based on the use of the prolate functions," in *Progress in Optics*, vol. IX, E. Wolf ed. (North-Holland, Amsterdam, 1971), pp. 313-407.

[9] M. Bertero and E. R. Pike, "Resolution in diffraction-limited imaging, a singular value analysis: I. The case of coherent illumination," Opt. Acta, vol. 29, pp. 727-746 (1982).

[10] M. Bertero and C. De Mol, "Superresolution by data inversion," Progress in Optics, vol. XXXVI, pp. 129-178 (1996).

[11] C. Matson and D. Tyler, "Primary and secondary superresolution by data inversion," Opt. Express, vol. 14, pp. 456-473 (2006).

[12] H. Van Trees, *Detection, Estimation, and Modulation Theory* (Wiley, New York, 1968).

[13] P. Sementilli, B. Hunt, and M. Nader, "Analysis of of the limit of superresolution in incoherent imaging," J. Opt. Soc. Am. A, vol. 10, pp. 2265-2276 (1993).

[14] G. Arfken and H. Weber, *Mathematical Methods for Physicists* (Elsevier, Amsterdam, 2005), 6th edition, Chap. 11.

[15] X. Luo and S. Prasad, in preparation.